Quantum-State-Resolved CO_2 Scattering Dynamics at the Gas−Liquid Interface: Dependence on Incident Angle†

Bradford G. Perkins, Jr. and David J. Nesbitt*

JILA, University of Colorado and National Institute of Standards and Technology, and Department of Chemistry and Biochemistry, University of Colorado, Boulder, Colorado 80309-0440

Received: February 1, 2007; In Final Form: May 1, 2007

Energy transfer dynamics at the gas−liquid interface have been probed with a supersonic molecular beam of CO_2 and a clean perfluorinated-liquid surface in vacuum. High-resolution infrared spectroscopy measures both the rovibrational state populations and the translational distributions for the scattered CO_2 flux. The present study investigates collision dynamics as a function of incident angle ($\theta_{inc} = 0°$, 30°, 45°, and 60°), where column-integrated quantum state populations are detected along the specular-scattering direction (i.e., $\theta_{scat} \approx \theta_{inc}$). Internal state rovibrational and Doppler translational distributions in the scattered CO_2 yield clear evidence for *nonstatistical* behavior, providing quantum-state-resolved support for microscopic branching of the gas−liquid collision dynamics into multiple channels. Specifically, the data are remarkably well described by a two-temperature model, which can be associated with both a trapping desorption (TD) component emerging at the surface temperature ($T_{rot} \approx T_S$) and an impulsive scattering (IS) component appearing at hyperthermal energies ($T_{rot} > T_S$). The branching ratio between the TD and IS channels is found to depend strongly on θ_{inc}, with the IS component growing dramatically with increasingly steeper angle of incidence.

I. Introduction

Energy transfer between a gas and surface is a central theme in the description of heterogeneous chemistry at the molecular level. The collision dynamics depend on the nature of the gas, the liquid, and the system as a whole.[1−19] Factors influencing the scattering dynamics include the mass, internal degrees of freedom, and the chemical structure of the gas projectile, as well as the composition, temperature, and surface structure of the liquid. In terms of the gas−liquid interface, the energy transfer process is influenced by collision energy,[2,3,17] impact orientation,[5,11] and various long- and short-range electrostatic interactions.[7] In our previous studies of gas−liquid collisions, energy transfer from incident translation into the projectile's internal states has been investigated via molecular scattering from several liquids over a range of incident energies,[17] where high-resolution absorption spectroscopy has been used to measure both quantum state populations and translational distributions for the scattered CO_2. In the present work, we use this same technique to explore effects of the incident angle (θ_{inc}) on the scattering of CO_2 from a perfluorinated polyether (PFPE) liquid[20] in an effort to elucidate the important parameters in gas−liquid scattering dynamics at the quantum-state-resolved level.

Many molecular beam experiments have probed the effects of incident angle on gas−liquid scattering. Sinha and Fenn first scattered atomic Ar off glycerol over a range of incident angles and energies.[21] At low incident energies (E_{inc}), the scattered argon flux follows a $\cos(\theta_{scat})$ distribution independent of θ_{inc}, indicative of thermal accommodation between the gas and surface. As E_{inc} increases, however, the measured flux begins to peak at specular-scattering directions (i.e., $\theta_{scat} \approx \theta_{inc}$), which is characteristic of a more impulsive interaction from a relatively flat surface. In an effort to uncover the mechanistic details of gas−liquid scattering, the Nathanson group has examined a variety of experimental parameters,[1−11] including the dependence on incident angle for several rare gas−PFPE systems.[5,11] These experiments reveal a complex manifold of dynamic processes, where the incoming molecules can scatter through a variety of pathways on the surface. As depicted in Figure 1, a simple physical picture has developed that successfully identifies two qualitatively different classes of collision dynamics: trapping desorption (TD) and impulsive scattering (IS). The TD pathway refers to incident molecules that lose enough energy to physisorb transiently to the surface or even momentarily dissolve into the liquid. The distinguishing feature is that the duration of such TD interactions is long enough for thermal accommodation, resulting in energy distributions for the desorbed species that are in equilibrium with the surface temperature (T_S). By way of contrast, molecules in the IS channel interact with the surface by one or relatively few collisions, which permits a significant fraction of the incident energy to be retained in the nonthermal-scattering distributions.

Within the context of this physical picture, experimentalists have investigated the competition between IS versus TD scattering channels as a function of incident angle. Using time-of-flight mass spectrometry (TOFMS), molecular beams have been scattered off liquid surfaces to explore final translational and angular distributions. Incident projectiles have ranged from atomic to polyatomic,[1] polar to nonpolar,[2,3] and closed-shell to radicals.[14] Likewise, surfaces of interest have included hydrocarbon,[2,13] hydrogen bonding,[2,9,10] perfluorinated,[3−5,11] ionic,[22−24] and metallic liquids,[8,25] as well as self-assembled monolayer surfaces (SAMs).[26−33] Gas flux measured over a range of scattering angles reveals a bimodal angular distribution that corresponds to TD and IS components.[5,11,14,30,32] As illustrated in Figure 1, the TD flux of molecules desorbs with a $\cos(\theta_{scat})$ distribution while the IS component follows an

† Part of the "Roger E. Miller Memorial Issue".

* Corresponding author. E-mail: djn@jila.colorado.edu.

10.1021/jp0709048 CCC: $37.00
Published on Web 06/20/2007

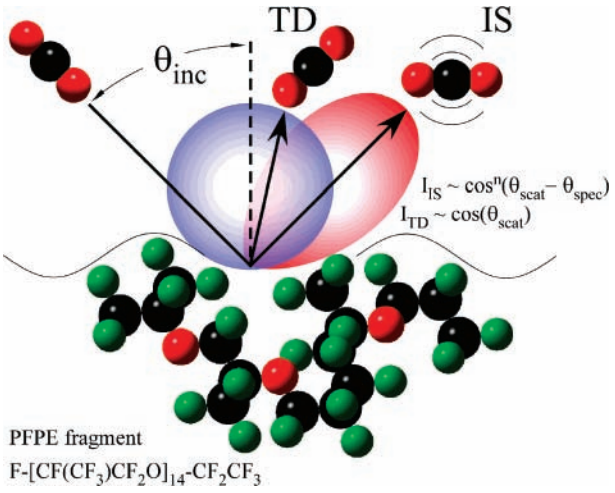

Figure 1. Schematic picture for CO_2 scattering from liquid perfluoropolyether (PFPE) as a function of incident angles, sampling (i) impulsive scattering (IS) and (ii) trapping desorption (TD) channels.

$\approx\cos^n(\theta_{scat} - \theta_{spec})$ pattern, with n typically greater than unity. Results from these experiments clearly show a conversion from diffuse to lobular scattering, indicative of a decrease in energy transfer as the angle of incidence increases.

In parallel with experimental investigations, theoretical efforts have exploited the combination of high-quality gas−surface potentials with molecular dynamics simulations to further elucidate the fundamental scattering interactions.[28−40] Results of these simulations capture many of the experimentally observed trends, including final angular, translational, and rotational state distributions largely consistent with a simple dual-channel scattering mechanism (i.e., TD and IS). However, these theoretical studies also reveal that what has been experimentally classified as the IS pathway can in fact reflect one, two, or even more collisional interactions at the gas−liquid interface. Of particular relevance to the current work, the presence of such *multiple* collisions in the IS channel provides opportunities for greater energy exchange between translational and rotational degrees of freedom, achieving Boltzmann-like distributions characterized by hyperthermal temperatures in excess of T_S.[36,37,39] Simply stated, the opportunity for additional collisional interactions in what is nominally an impulsive scattering event promotes a more microcanonical sampling of energies, thus yielding a hot, albeit thermal, internal state distribution in the scattering flux.

In addition to the TOFMS experiments, laser-based detection schemes have investigated gas−surface scattering dynamics to determine the importance of the projectile's internal degrees of freedom. Quantum-state-resolved studies examine not only the exchange of energy from the gas to the surface, but also the conversion of energy to rotation and vibration within the projectile. The majority of state-resolved work has focused on gas−solid scattering of molecules off metallic,[41−50] ionic,[51−54] and organic monolayer surfaces.[75] In systems such as N_2 and HCl scattering from Ag(111)[41] and Au(111),[46] respectively, only $\approx$20% of the incident translational energy is transferred to the surface. In both cases, the internal populations exhibit a "rotational rainbow" structure peaking at high J-states that has been qualitatively modeled by rigid-rotor hard-cube simulations.[55−61] In contrast to the very physically motivated impulsive mechanism for rotational excitation, vibrational energy transfer is considerably less efficient. This has been dramatically illustrated by elegant studies in Roger Miller's group of acetylene (C_2H_2) scattering from LiF(100).[52] Specifically, comparison between angular distributions for the asymmetric CH stretch excited and ground state molecules indicates that acetylene largely retains its vibrational energy throughout the scattering event. This retention of vibration holds true even under incident energy conditions that primarily yield the TD channel, indicating vastly different time scales for thermal accommodation of translation and rotation compared to vibration. Such pioneering efforts in quantum-state-resolved dynamics in gas−solid scattering provide a particularly interesting perspective for analogous state-resolved collision experiments at the gas−liquid interface.

In this work, we investigate the incident angle dependence of the scattering dynamics of CO_2 from perfluorinated polyether (PFPE), with full quantum state resolution of the scattered species. The results continue to build on previous studies in our group of CO_2 with low vapor pressure liquids, where a dual-channel (i.e., TD and IS) description of the collision dynamics has been validated for a series of incident energies. We have chosen specifically to focus on CO_2 scattering from PFPE liquids at high incident energy (E_{inc} = 10.6(8) kcal/mol). Previous studies have shown that the heavy CF_2/CF_3 groups in PFPE absorb less energy than the lighter CH_2/CH_3 groups in squalane and OH groups in glycerol,[2,3,17] thereby decreasing the TD fraction [$\alpha = f_{TD}/(f_{IS} + f_{TD})$]. Furthermore, this TD fraction has also been shown to decrease with increasing E_{inc},[2,3,7,17] corresponding to more impulsive interactions with the surface. The current experiment explores specular-scattering geometries for incident impact angles that range from normal incidence to 60° off axis. The results provide an opportunity to further test and explore the two-temperature model developed in previous efforts, whereby the scattered rotational distributions were surprisingly well characterized by a linear combination of a (i) room-temperature TD component and a (ii) hyperthermal, yet Boltzmann-like, IS component. Results and analysis can also be compared to TOFMS experiments for similar systems to gain further insight into the mechanistic details of gas−liquid scattering at the molecular level.

The remaining sections of the paper are organized as follows. Section II describes the geometric configuration of the molecular beam, liquid surface, and infrared spectrometer. Section III includes the incident beam characterization, along with the internal state populations and translational distributions for the specular scattering of CO_2 from PFPE. A discussion of the results presented in section IV includes further analysis of the energy transfer. A summary of the results and final conclusions are included in section V.

II. Experimental Section

The essential experimental details include an incident molecular beam of supersonically cooled molecules, a clean liquid surface in high vacuum, and a Pb salt diode laser spectrometer to detect the scattered projectiles. Each of these components has been described in previous papers.[17,19] In this section, therefore, we focus only on details specific to the present experiment, specifically emphasizing the experimental modifications required to achieve a tunable angle of incidence and detection.

Figure 2 shows the range of configurations used to study the effects of incident angle on the scattering dynamics of CO_2 and liquid PFPE. While our previous studies have focused on scattering at normal incidence, the current geometrical setup has been modified to probe incident angles that range from 0° to 60°. The incident scattering and detection angles depend upon the geometrical arrangement of the molecular beam, liquid surface, and laser beam. We define the liquid surface as the

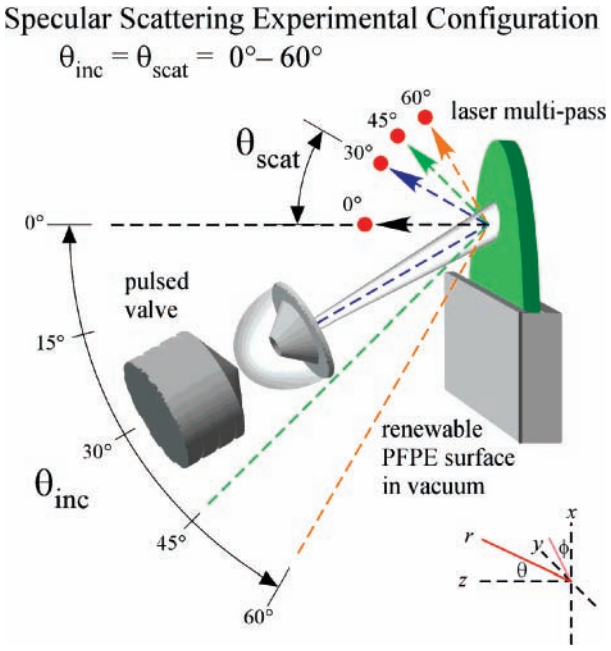

Figure 2. Schematic-scattering geometry used in the current study, where θ_{inc} is the tunable polar angle with respect to the surface normal. A Pb salt diode laser spectrometer is used to extract internal rovibrational state populations (v,J) and translational distributions (v_y) from the scattered CO_2.

$x-y$ plane, where the z-axis corresponds to normal incidence ($\theta_{inc} \approx 0°$) and the origin is the point at which the centerline of the molecular beam intersects the surface. While Cartesian coordinates correspond most naturally to laser characterization of the Doppler components, spherical coordinates provide a more simplified description of the scattering geometries. Therefore, both coordinate systems will be used as needed in the experimental description and analysis of the results.

The incident molecular beam is prepared by supersonically expanding a 10% mixture of CO_2 in H_2 through a 500 μm pinhole with a pulsed valve based on the designs of Proch and Trickl.[62] As shown in Figure 2, the valve pivots on an arm around the origin for $\theta_{inc} = 0°-60°$ at a fixed pinhole-to-surface distance (d = 10 cm) for each incident angle. A 5.0 mm skimmer is positioned 2.5 cm downstream of the pinhole to restrict the spread of the centerline incident angle to $\pm 6°$. The pinhole, skimmer center, and origin are aligned optically with a visible diode laser to optimize the beam collimation and fix the incident direction. The CO_2/H_2 gas pulse is 400 μs in duration and impinges upon a fresh PFPE surface in the vacuum, which is generated using the methods of Lednovich and Fenn[63] where a 12.7 cm glass wheel is partially submerged in a 300 mL PFPE reservoir and rotates at 0.5 Hz through the liquid. As the wheel emerges from the reservoir, a 6 cm stainless-steel razor blade scrapes away the topmost layer of the liquid to remove any surface impurities, permitting a freshly renewed surface to rotate into the path of the molecular beam. The wheel assembly is housed in a 60 L aluminum vacuum chamber, where a 6 in. liquid nitrogen trapped diffusion pump maintains an average pressure of $\approx 3 \times 10^{-5}$ Torr with pulsed valve operation at 11 Hz and stagnation pressures of 100 Torr.

High-resolution laser absorption spectroscopy is used to probe the J-state populations of the incident molecular beam and scattered flux. A narrow-band Pb salt diode laser generates $\approx 1-2$ μW of tunable infrared light around $\lambda = 4.2$ μm, where the frequency is tuned by temperature ($3-4$ cm^{-1}/K) and current (≈ 2 MHz/μA). The laser output is split into several beams within the spectrometer. Approximately one-third of the collimated laser beam is passed into the vacuum chamber and travels parallel to the liquid surface in a 16-fold multipass configuration.[64] Orientation of the laser beam with respect to the origin on the surface defines the detection angle for the scattered CO_2 flux. The beam is passed parallel to the liquid surface such that the origin-to-beam distance is 2 cm at $\varphi = 0°$ and $\theta_{inc} = \theta_{scat}$. After the multipass, the transmitted laser beam is focused onto a liquid N_2 cooled InSb signal detector. A second fraction of the laser beam is directly focused onto a matched InSb reference detector, where fast servo-loop-stabilized subtraction of signal and reference beams is used to eliminate common mode noise on the laser light. The subtraction scheme achieves absorption sensitivities of $(1-2) \times 10^{-6}$ Hz$^{-1/2}$, which is within a factor of 2 of the shot noise limit for the ≈ 0.5 μW of laser power on each detector. The remaining fraction of laser light is used in conjunction with a CO_2 reference gas cell and transmission etalon to determine the absolute and relative frequency throughout the duration of a laser scan.[17,19]

Data acquisition includes recording the transient absorption pulse as a function of frequency for a series of CO_2 rovibrational transitions. The laser is scanned in 2 MHz steps over a given Doppler-broadened transition. At each frequency, a 2000 μs sample of the transient signal is recorded to encompass times before, during, and after arrival of the gas pulse at the surface. The full temporal trace is stored for each frequency step to provide opportunity to analyze the scattered CO_2 populations either (i) as a direct function of time for a particular Doppler detuning, or (ii) as a function of frequency for signals integrated in the time domain. Data analyzed and presented in this paper represent integration of the time-dependent signal over a fixed window to generate a frequency-dependent Doppler profile, where the 200 μs temporal gate spans the 25−75% rising edge region of the transient gas pulse. More importantly, this time window is sufficiently short to prevent background contamination from reentering the laser beam path that may have collided and equilibrated with the walls of the chamber.

As we analyze the measured absorption signals from the scattered flux, we need to consider several details about the incident and scattering angles created by the geometrical arrangement of the molecular beam, liquid surface, and laser beam. The angle of incidence is well-defined by the polar angle between the surface normal and the centerline of the molecular beam. The scattering angles, however, include a range of directions because the laser beam detects both in-plane ($\varphi_{scat} = 0°$) and out-of-plane ($\varphi_{scat} \neq 0°$) trajectories. Each absorption profile at a given detuning frequency ($\nu - \nu_0$) represents the density of $CO_2(v,J)$ with a specific velocity component parallel to the laser beam, i.e., $v_y = v \sin(\theta_{scat}) \sin(\varphi_{scat})$, where $\nu - \nu_0 = \nu_0 v_y/c$. In-plane scattering events (i.e., $v_y = 0$) are therefore detected at the centerline transition frequency (ν_0), while out-of-plane trajectories are sampled as a function of Doppler detuning along the laser path. Although the column-integrated detection geometry samples a finite range in θ_{scat} and φ_{scat}, the additional capability of high-resolution Dopplerimetry provides novel information on both in-plane and out-of-plane scattering events.

III. Results and Analysis

A. Molecular Beam Characterization. The incident molecular beam of CO_2 is fully characterized at the beginning of each scattering experiment. Populations in the ground state (00^00) and vibrational hot band (01^10)[65] are probed with the diode laser spectrometer in the absence of the liquid wheel assembly. The internal state distributions are extracted from the

TABLE 1: Properties of the Incident Molecular Beam and Bulk PFPE Liquid

PFPE		incident molecular beam	
chemical composition	$F-[CF(CF_3)CF_2O]_{14}{}^a-CF_2CF_3$	gas mixture	10% CO_2 in H_2
mass	2400 amu[a]	θ_{inc}	0°, 30°, 45°, 60°
density	1.87 g/cm^3	E_{inc}	10.6(8)[d] kcal/mol
melting point	−45 °C	T_{rot} (00^00)	19(3) K
boiling point	200 °C	T_{rot} (01^10)	15(4) K
vapor pressure	7×10^{-7} Torr[b]	T_{vib}	175(10) K
viscosity	80 cp[b]	v_z	$1.41(9) \times 10^5$ cm/s
compressibility	10^{-9} cm^2/dyn	$\Delta\nu_D$	63(2) MHz
surface tension	17 dyn/cm		
K_H	3.1×10^4 Torr[c]		

[a] Average size of Krytox 1506 polymer. [b] At 25 °C. [c] Henry's law constant for CO_2 with $C_{10}F_{22}O_2$. [d] Number in parentheses indicates 1σ for multiple measurements.

series of absorption profiles in both vibrational manifolds, where the absorption profile represents the CO_2 density at a particular Doppler-detuning frequency. Integration of the absorption profiles over all Doppler-detuning frequencies generates a column-integrated density ($A_{v,J}$) to capture the entire population in a particular quantum state. Each $A_{v,J}$ is scaled by the appropriate Hönl−London factor (S_J), degeneracy ($2J+1$), and then plotted logarithmically against $E_{rot} = B_{CO_2}J(J+1)$, where the slope of the best-fit line characterizes the rotational temperature (T_{rot}). The rotational states for both the 00^00 and 01^10 manifolds are cooled to $T_{rot} \approx 15-20$ K, and include minor "freeze-in" effects[66,67] for high rotational states in the pinhole expansion. A characteristic vibrational temperature is extracted from the ratio of the total populations in the 00^00 and 01^10 manifolds. The degenerate-bending mode of CO_2 is only partially cooled to $T_{vib} \approx 175$ K, which once again illustrates the difficulty in relaxing large quanta of energy (667 cm^{-1}) in a pinhole expansion.[66,67]

The translational distributions in the incident molecular beam are measured with a microphone time-of-flight technique and Dopplerimetry analysis of the absorption profiles. First, the centerline velocity is measured with a hearing-aid microphone in a time-of-flight configuration[68] where the gas pulse arrival time is measured for a series of downstream distances. A simple distance versus time plot reveals the centerline velocity (v_{beam}= $1.41(9) \times 10^5$ cm/s), which agrees quite well with a calculated velocity ($v_{beam} = 1.42 \times 10^5$ cm/s) based on simple gas-flow formulas.[66] In addition to the centerline velocity, Dopplerimetry analysis of the absorption profiles extracts the transverse velocity distributions since the molecular beam is perpendicular to the laser beam. Each Doppler profile is fit with a Voigt line shape function in a nonlinear least squares fitting algorithm. The Gaussian component [$\Delta\nu_D = 63(2)$ MHz] characterizes the transverse translational distribution of the skimmed molecular beam, while the Lorentzian component accounts for the residual line width of the diode laser ($\Delta\nu_L \approx 20$ MHz) due to current noise. Since the pinhole expansion is symmetric about the centerline axis, the extracted Doppler widths characterize both the *x*- and *y*-transverse velocities. The results of the molecular beam characterization are summarized in Table 1.

B. Incident Angle Dependence of CO_2 + PFPE: Internal State Distributions. High-resolution absorption profiles of rotational states within the 00^00 and 01^10 manifolds have been measured for scattered CO_2 off PFPE over a range of incident angles at $E_{inc} = 10.6(8)$ kcal/mol. Sample absorption profiles are shown in Figure 3 for $\theta_{inc} = \theta_{scat} = 30°$ and 60° to illustrate the qualitative differences observed in the scattering distributions as a function of incident angle. The rotational state populations shift from low to high *J*-states as the incident angle is increased from 30° to 60°. Nonthermal dynamics are also apparent within each *J* level. Specifically, the absorption profile Doppler widths

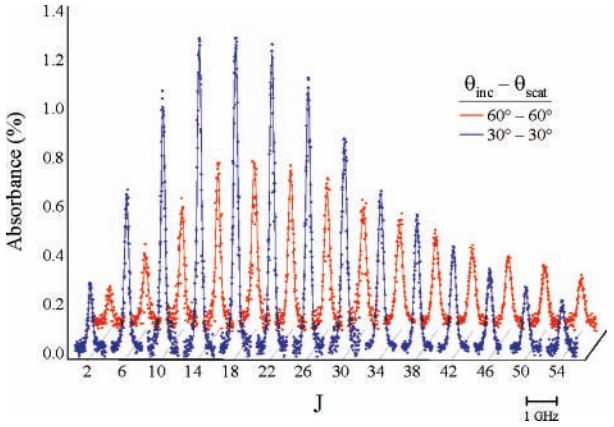

Figure 3. Sample data illustrating measured absorption profiles for two different incident angles. The solid line represents the line shape fit from the Dopplerimetry analysis described in section IIIC.

systematically *increase* with rotational state, a trend that has been observed in other CO_2−liquid scattering systems.[17] Internal state and Dopplerimetry analyses of these absorption profiles provide a quantitative description of the incident angle effects in terms of the observable non-Boltzmann scattered flux distributions.

The Boltzmann analysis of the scattered flux populations parallels the scheme outlined for the molecular beam characterization in section IIIA. The absorption profiles are integrated to column densities ($A_{v,J}$) to represent the total quantum state population that has been detected over the range of φ_{scat} and fixed θ_{scat} angles. Since the incident molecular beam overlaps in time and space for $\theta_{inc} = 0°$, the scattered flux populations for $\theta_{scat} = 0°$ have been corrected for minor incident beam contamination caused by the "freeze-in" effects of the pinhole expansion. However, no corrections are necessary for any of the nonnormal trajectories, $\theta_{inc} = 30°-60°$, since the incident-skimmed molecular beam completely misses the laser on the path from the pinhole to the surface. Once the appropriate adjustments have been made, each column density is scaled by S_J and $2J+1$ and then plotted in the standard Boltzmann fashion. The sample plot in Figure 4 shows clear curvature in the population distributions for each incident angle. Similar non-Boltzmann distributions have been measured for other scattering conditions, all of which have been characterized with a two-temperature Boltzmann function.[17−19,36,37,39,69]

The two-temperature Boltzmann analysis partitions the scattering into two channels: trapping desorption (TD) and impulsive scattering (IS). The analysis is based on describing the total population as the sum of the TD and IS components, where the quantum state distribution of each subpopulation is well characterized with a rotational temperature, T_{rot}(TD/IS). The model assumes that molecules scattering through the TD channel

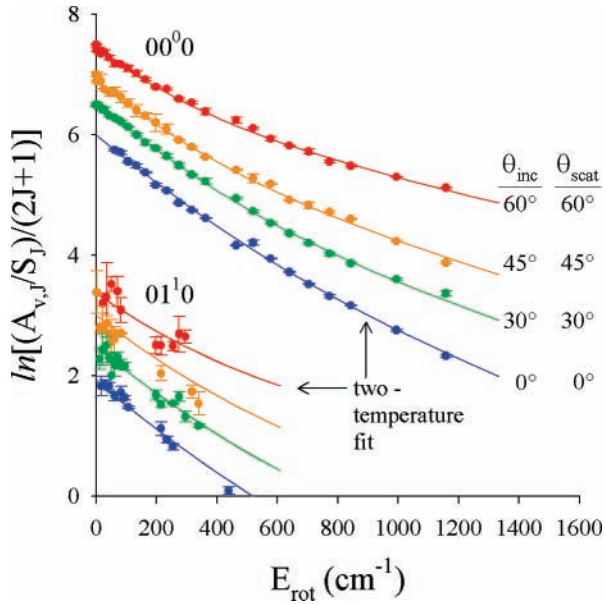

Figure 4. Sample Boltzmann plots for $\theta_{inc} = \theta_{scat} = 0°$, 30°, 45°, and 60°. Non-Boltzmann distributions are observed at each incident angle. The populations are well modeled as the linear combination of TD and IS components, where each subpopulation is described by a rotational temperature, T_{rot}(TD/IS).

thermally accommodate with the surface, thereby desorbing with $T_{rot}(TD) \approx T_S \approx 298$ K. The quantum state populations are fit to the following two-temperature Boltzmann function:

$$\frac{A_{v,J}}{S_J} = P_{v,J} = N\{\alpha P_{TD}(J) + (1-\alpha)P_{IS}(J)\}P_{vib}(v) \quad (1)$$

where N is a normalization constant and α is the fraction of molecules in the TD channel. $P_{TD/IS}(J)$ and $P_{vib}(v)$ are the normalized standard rotation and vibration Boltzmann probabilities:

$$P_{TD/IS}(J) = \frac{(2J+1)e^{-E_{rot}/kT_{rot}(TD/IS)}}{Q_{rot}(TD/IS)} \quad (2)$$

$$P_{vib}(v) = \frac{e^{-hv/kT_{vib}}}{Q_{vib}} \quad (3)$$

The scaled column densities for both the 00^00 and 01^10 manifolds are simultaneously fit to extract α, T_{rot}(IS), and T_{vib}, where T_{rot}(TD) is fixed at 298 K to help minimize parameter correlation. The extracted parameters for all incident angles are listed in Table 2.

The results from the two-temperature fit are used to normalize the scattered quantum state populations for the 00^00 and 01^10 vibrational manifolds. The fractional populations are reported in Table 3 and plotted in Figure 5, which includes the two-temperature fit that nicely accounts for the non-Boltzmann behavior. In addition, the individual TD and IS components have been plotted to qualitatively show the fractional partitioning of the two scattering channels. Arrows on the plot indicate the rotational state where the TD contribution to the total $A_{v,J}$ is 50%. As θ_{inc} increases, the arrows progressively shift to lower rotational states, indicative of a higher fraction of IS population in the total scattered flux. The fractional hot-band populations ($\times 10$) have been plotted to illustrate the independence of rotational and vibrational excitation. The 01^10 populations are well fit by the two-temperature Boltzmann function, which thereby characterizes the vibrationally excited CO_2 with T_{rot}-(TD/IS) rotational temperatures. Parallel structure in the scattering dynamics between the ground state and hot band once again illustrate the efficiency of energy flow into rotation, but not into vibration.

The parameters within the two-temperature Boltzmann fit provide the opportunity to test the effects of incident angle against physical intuition. First of all, the TD fraction (α) for CO_2 has been plotted in Figure 6a as a function of $\theta_{inc}/\theta_{scat}$. The values for α decrease from 0.54 to 0.29 as θ_{inc} increases from 0° to 60°, which is qualitatively consistent with the range of gas−liquid studies outlined in section I where the TD fraction drops as energy transfer becomes less efficient. In terms of a simple hard-cube collision,[56] energy exchange between the gas and surface depends upon only the normal component of the projectile's momentum. Within this framework, the projectile retains a larger fraction of E_{inc} as θ_{inc} increases since the incident momentum shifts from the normal to parallel direction, thereby decreasing the trapping probability.

In addition to the TD fraction (α), the characteristic rotational temperatures provide further insight into the energy transferred during impact. T_{rot}(IS) and T_{vib} are plotted in Figure 6b, also as a function of $\theta_{inc}/\theta_{scat}$, to illustrate two important trends. First, T_{rot}(IS) ranges from 720(30) K at normal incidence to 1220-(40) K at $\theta_{inc} = 60°$, which clearly indicates that the scattered CO_2 retains more of E_{inc} in the rotational degree of freedom for glancing versus normal incident collisions. In contrast to the extensive rotational excitation, T_{vib} remains relatively constant at a *subthermal* temperature of ≈240 K. Although T_{vib} increases from ≈175 K in the molecular beam, the cold-scattering temperature reveals the lack of translational-to-vibrational energy transfer in the collision. Such a trend nicely complements the vibrational energy transfer studies of Miller and co-workers for C_2H_2 scattering from LiF(100),[52] which indicated CH stretch excitation to be effectively decoupled from collision dynamics. This is perhaps even more surprising for the CO_2 bend vibration (667 cm^{-1}), which has a further 5-fold reduction in frequency from the asymmetric CH stretch in C_2H_2. Nevertheless, the clear contrast between internal state excitation in $CO_2(v,J)$ illustrates that TD and IS interactions are both limited to time scales where translational energy can transfer to rotation, but not to vibration.

C. Incident Angle Dependence of CO_2 + PFPE: Translational Distributions. The narrow bandwidth of the diode laser spectrometer provides a way to determine the translational distributions for the scattered flux of CO_2. A general Doppler-imetry analysis of the absorption profiles has been outlined in section IIIA, where the line shape analysis extracts the translational distributions for the scattered CO_2 in a direction parallel to the laser beam. As discussed in the previous section, the laser detection scheme is only sensitive to the v_y component of the scattered velocity distribution. Analysis of this component, however, provides complementary physical insight into the two-temperature description of the TD- and IS-scattered populations.

The Doppler-broadened line shapes are first fit with a Voigt line shape function that uses a nonlinear least squares fitting algorithm. The Gaussian component ($\Delta\nu_D$) of the Voigt line shape reflects a Maxwellian velocity distribution that is characterized by a single translational temperature, T_{trans}, with a small Lorentzian component accounting for residual diode laser line width contributions to the overall Doppler profile. Absorption profiles for the 00^00 manifold are fit to extract T_{trans} as a function of J for all the incident energies, which are listed in Table 4. $T_{trans}(J)$ values are plotted in Figure 7 to show the J-state

TABLE 2: Two-Temperature Boltzmann and Dopplerimetry Analysis

θ_{inc} (deg)	θ_{scat}[a] (deg)	α	T_{rot}(IS) (K)	T_{trans}(IS) (K)	T_{vib} (K)	$\langle E_{scat}\rangle/E_{inc}$	$\langle E_{scat}(IS)\rangle/E_{inc}$
0	0	0.54 (3)[b]	720 (30)	850 (30)	235 (5)	0.30 (3)	0.45 (4)
30	30	0.51 (3)	860 (40)	880 (50)	237 (5)	0.33 (3)	0.49 (4)
45	45	0.42 (3)	945 (60)	1120 (60)	247 (5)	0.42 (4)	0.60 (5)
60	60	0.29 (2)	1220 (40)	1130 (80)	238 (9)	0.51 (4)	0.65 (6)

[a] θ_{scat} reflects the specular angle in the $x-z$ scattering plane [b] Numbers in parentheses represent the estimated error from the two-temperature fit over several data sets.

TABLE 3: Quantum-State-Resolved CO_2 Populations

$\theta_{inc}-\theta_{scat}$							
0°−0°		30°−30°		45°−45°		60°−60°	
J	population	*J*	population	*J*	population	*J*	population
00^00 *J*-State Populations ($\times 10^{-2}$)[a]							
0	—[b]	0	0.25 (1)[c]	0	0.26 (1)	0	0.19 (1)
2	—	2	1.24 (1)	2	1.14 (2)	2	0.86 (3)
4	—	4	2.23 (1)	4	2.08 (5)	4	1.55 (7)
6	—	6	3.07 (4)	6	3.0 (3)	6	2.12 (1)
8	—	8	3.9 (2)	8	3.41 (9)	8	2.85 (9)
10	—	10	4.41 (9)	10	4.0 (3)	10	3.2 (1)
12	5.4 (1)	12	5.03 (9)	12	4.8 (3)	12	3.4 (2)
14	6.0 (2)	14	5.5 (1)	14	5.1 (5)	14	3.94 (8)
16	5.90 (8)	16	5.70 (2)	16	5.2 (4)	16	4.2 (2)
18	6.2 (2)	18	5.64 (9)	18	5.2 (5)	18	4.3 (2)
20	6.14 (9)	20	5.5 (2)	20	5.3 (2)	20	4.4 (1)
22	5.5 (1)	22	5.5 (1)	22	5.2 (4)	22	4.22 (8)
24	5.42 (9)	24	5.2 (2)	24	5.1 (4)	24	4.29 (9)
26	4.79 (8)	26	4.8 (1)	26	4.57 (3)	26	4.07 (7)
28	4.55 (3)	28	4.46 (4)	28	4.37 (8)	28	4.1 (1)
30	4.29 (2)	30	4.3 (2)	30	3.98 (5)	30	3.8 (1)
34	3.40 (2)	34	3.65 (8)	34	3.62 (7)	34	3.5 (2)
36	3.15 (9)	36	3.11 (6)	36	3.3 (2)	36	3.22 (5)
38	2.76 (2)	38	2.70 (3)	38	3.21 (4)	38	3.05 (9)
40	2.32 (2)	40	2.39 (4)	40	2.57 (2)	40	2.87 (1)
42	1.99 (2)	42	2.14 (4)	42	2.5 (1)	42	2.72 (9)
44	1.71 (5)	44	1.88 (6)	44	2.32 (5)	44	2.42 (4)
46	1.53 (1)	46	1.67 (3)	46	2.16 (3)	46	2.34 (5)
50	1.10 (2)	50	1.39 (3)	50	1.62 (3)	50	2.13 (1)
54	0.78 (2)	54	1.19 (5)	54	1.23 (3)	54	1.91 (3)
01^10 *J*-State Populations ($\times 10^{-4}$)							
6	5.6 (9)	5	4.0 (7)	2	3.4 (12)	5	5.4 (31)
8	7.6 (5)	7	6.5 (17)	5	4.2 (3)	7	3.9 (6)
10	9.0 (6)	9	8.7 (12)	7	5.6 (21)	9	5.4 (31)
12	9.1 (7)	10	7.8 (6)	9	7.7 (10)	11	8.1 (9)
13	9.6 (4)	11	6.4 (18)	10	7.2 (4)	13	8.5 (21)
14	11 (1)	12	8.3 (2)	11	7.0 (26)	14	6.7 (14)
16	10.0 (2)	13	10.1 (9)	12	7.9 (16)	22	5.8 (8)
21	9.1 (11)	14	9.8 (7)	13	9.3 (6)	23	6.0 (9)
23	7.4 (4)	15	10.1 (6)	14	10.1 (1)	25	6.4 (5)
24	8.7 (5)	22	9.1 (8)	23	8.4 (11)	26	8.2 (24)
31	4.8 (3)	23	8.1 (4)	28	7.5 (8)	27	8.1 (9)
38	2.7 (5)	25	8.9 (1)	29	6.4 (12)		
		26	10.4 (8)				
		27	7.8 (7)				
		29	7.1 (2)				

[a] Normalized to total populations predicted from the two-temperature analysis described in section III. [b] Low *J*-state populations are not reported because of contamination from the incident molecular beam. [c] Values in parentheses represent 1σ for multiple measurements.

dependence on translational distributions, where T_{trans} increases with *J* for all incident angles. These same trends have been observed in our incident energy studies of CO_2,[17,19] which lead to a two-temperature line shape analysis to describe the trend in $T_{trans}(J)$ in terms of a shift in the line shape contributions from TD to IS at higher *J*-states.

The two-temperature line shape analysis parallels the development of the two-temperature Boltzmann function described in section IIIB. The analysis is based again on describing the total absorption profile as the sum of individual TD and IS line shapes, where each component is modeled with a Voigt function and common $\Delta\nu_L$. The two Gaussian components characterize the translational distribution for each channel with a temperature T_{trans}(TD/IS). The total line shape is

$$S_J(\nu-\nu_0) = N\{\alpha_J g_{TD}(\nu-\nu_0) + (1-\alpha_J) g_{IS}(\nu-\nu_0)\} \quad (4)$$

where α_J is the fraction of TD molecules per *J*-state

$$\alpha_J = \frac{\alpha P_{TD}(J)}{\alpha P_{TD}(J) + (1-\alpha) P_{IS}(J)} \quad (5)$$

with probabilities $P_{TD/IS}(J)$ defined by eq 2. We again assume that the TD component has reached thermal equilibrium with

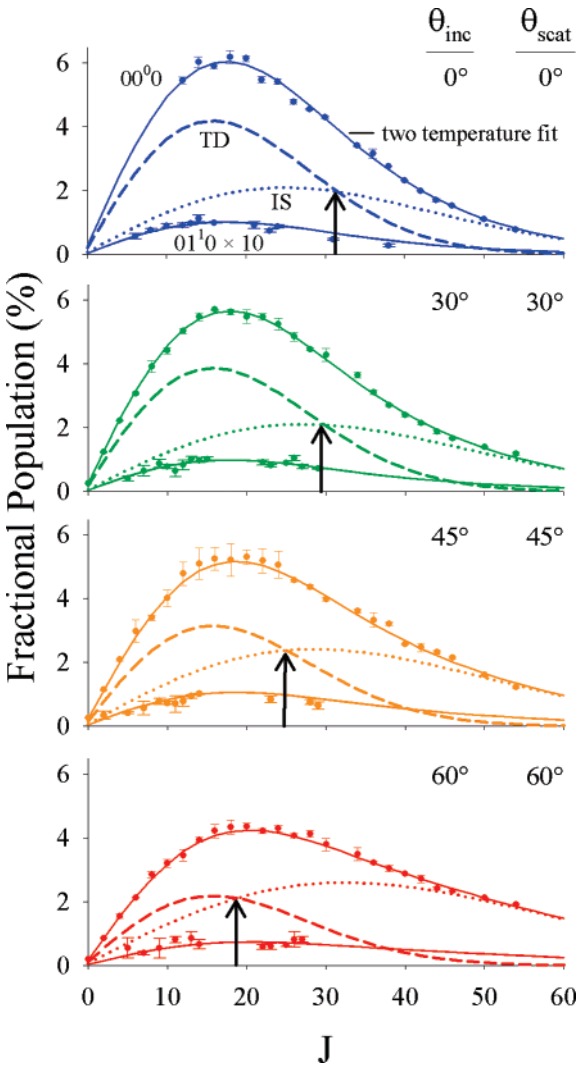

Figure 5. Fractional populations for both 00^00 and 01^10 manifolds, plotted with the two-temperature TD/IS Boltzmann fits described in section IIIB. Note that the 01^10 populations have been magnified by an order of magnitude.

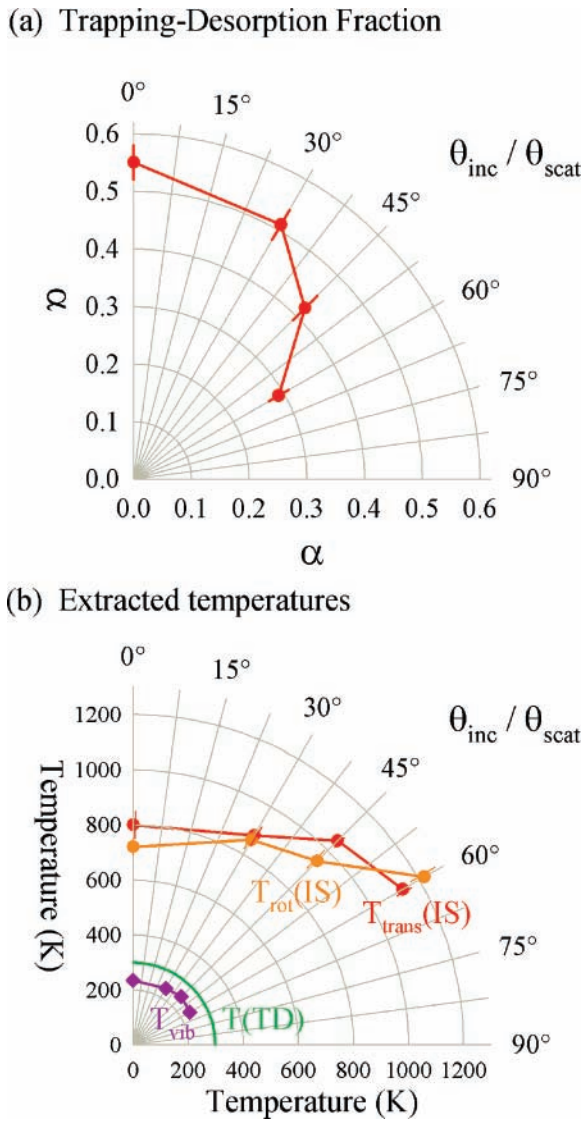

Figure 6. Two-temperature fit parameters for each incident angle: (a) trapping desorption fraction (α) and (b) translational, rotational, and vibrational temperatures of the scattered CO_2, plotted as a function of $\theta_{inc}/\theta_{scat}$.

the surface so that T_{trans}(TD) is held fixed at $T_S \approx 298$ K. Values of α_J are calculated from the parameters listed in Table 2. The α_J values and fixed TD width allow us to determine the amplitudes of both the TD and IS components. Armed with this information for each J-state, we can fit the Doppler profiles with the total line shape function to extract the full width at half-maximum (fwhm) of the IS component, which in turn yields an estimate for T_{trans}(IS). The robustness of this algorithm has been tested by analysis over a series of J-states; the extracted value of T_{trans}(IS) proves to be constant to within 5% over all J-state absorption profiles at a given incident angle.

The two-temperature line shape analysis provides a simple physical picture to describe the correlated $T_{trans}(J)$ values presented in Figure 7. The measured absorption profiles reflect the relative fraction of TD to IS populations. As the IS fraction increases toward unity at high rotational states, the IS translational distribution contributes more to the total absorption profile, thereby leading to an increase in width for the overall line shape. To illustrate how this width evolves, values for α, T_{trans}(TD/IS), and T_{rot}(TD/IS) have been used in eqs 4 and 5 to construct an empirical two-temperature line for each rotational state. These two-temperature line shapes are then fit with a single-temperature Gaussian function to extract $T_{trans}(J)$, which is plotted as a solid line in Figure 7 along the experimental data. The single-temperature fit of a two-temperature line shape agrees remarkably well with the experimentally determined values of $T_{trans}(J)$ for the scattered CO_2 absorption profiles.

IV. Discussion

The IS and TD components of the scattered CO_2 populations have been isolated with a two-temperature analysis of the internal state populations and the corresponding translational distributions. The two-temperature Boltzmann analysis reveals the balance between TD and IS scattering shifts from one to the other as the incident angle increases from 0° to 60°. As discussed in the Introduction, the mechanistic details of gas−liquid scattering depend upon the energy transferred during the interaction. In the following section, we calculate the fraction of energy transferred to the surface as a function of θ_{inc} to determine if the measured trends are consistent with a change in energy transfer. The estimated fraction of energy exchanged through the IS channel is also compared with atom−PFPE studies to illustrate the differences in scattering based on the internal degrees of freedom in CO_2. In addition, we compare the extent of rotational excitation between CO_2−PFPE and molecule−metal scattering to gain further insight into the similarities and differences between liquid and solid surfaces.

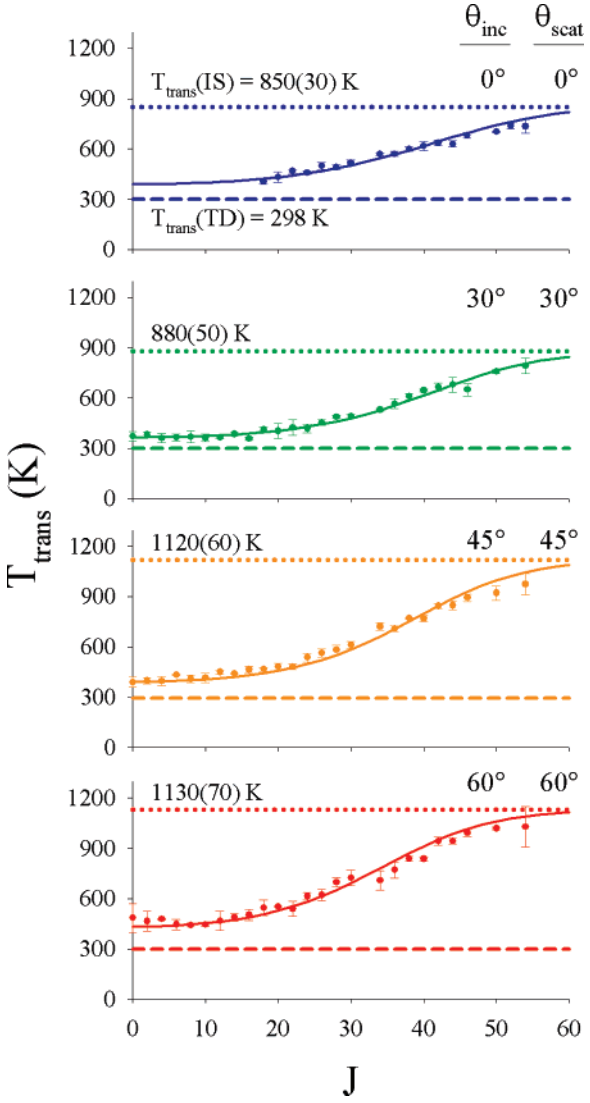

Figure 7. *J*-state-dependent translational distributions of scattered CO_2. A single-temperature line shape analysis yields $T_{trans}(J)$, while a two-temperature line shape extracts T_{trans}(IS). The solid line is a single Gaussian fit for a reconstructed two-temperature line shape (see text for details).

The total energy in the scattered CO_2 is calculated from the rovibrational state populations and the correlated translational distributions. Direct measurement of the rotational state distributions leads to the average internal energy, $\langle E_{v,J} \rangle$, of the scattered CO_2 flux. Since the progression of CO_2 states extends beyond the tuning capability of the diode laser spectrometer, this average internal energy, $\langle E_{v,J} \rangle$, is calculated by elementary statistical mechanics from the characteristic rotational and vibrational temperatures, T_{rot}(TD/IS) and T_{vib}. To include translational energy, T_{trans}(TD/IS) values are used from the high resolution Dopplerimetry analysis of the absorption profiles. Rigorously, the line shape analysis characterizes only one of the three velocity components, specifically v_y. The two additional velocity distributions, v_x and v_z, are estimated based on our physical model of the scattering system and previous studies of similar systems. Specifically, the total translational energy for the TD component is $2kT_{trans}$(TD) based on our assumption that the TD channel is characterized by diffuse thermal scattering.[70] Compared to the well-determined TD component, the two unknown IS velocities are estimated from the results of Hase and coworkers, where they show that the IS flux follows a $\cos(\theta_{scat})$ angular distribution for $\theta_{inc} = 0°$.[39] If this angular distribution

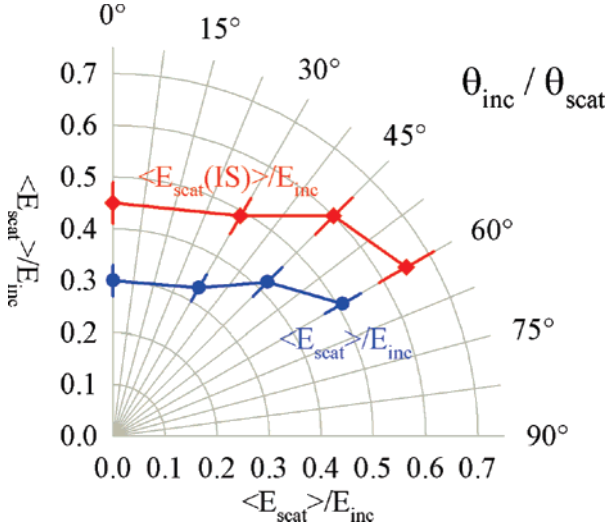

Figure 8. Fractional energy remaining in CO_2 after collision with the surface.

holds true over all the incident angles, then the total IS translational energy is $2kT_{trans}$(IS). Since angular distributions tend to shift toward lobular scattering as θ_{inc} increases,[14] the value of $2kT_{trans}$(IS) most likely represents a conservative *lower* limit for the total IS translational component. Even so, this assumption gives us an opportunity to compare the *total* energy retained in the CO_2 with other atomic projectiles, which is approximately

$$\langle E_{scat} \rangle \approx \alpha\{kT_{rot}(TD) + 2kT_{trans}(TD)\} + (1 - \alpha)\{kT_{rot}(IS) + 2kT_{trans}(IS)\} \quad (6)$$

where the IS fraction is

$$\langle E_{scat}(IS) \rangle \approx kT_{rot}(IS) + 2kT_{trans}(IS) \quad (7)$$

When divided by E_{inc}, the values are an estimate for the fraction of energy retained in the scattered CO_2. These fractions are listed in Table 2 and plotted in Figure 8 as a function $\theta_{inc}/\theta_{scat}$, where the trend clearly indicates a decrease in energy transfer as molecules impinge from larger angles.

From this analysis, the energy transfer and trapping probability for CO_2 colliding with PFPE parallel the general trends observed in atom + liquid scattering studies. Specifically, incident angle effects have been previously investigated with rare gas scattering of Ne, Ar, and Xe from PFPE at $\theta_{inc} = 25°$, 45°, and 65°.[5,11] Measurements of the scattered flux intensities show broad distributions as a function of final angle, where intensities peak toward specular angles. The general trends indicate that energy transfer is sensitive to both the incident and recoil angles of the gas projectile. For example, when scattered from PFPE at $E_{inc} = 19$ kcal/mol, argon atoms in the IS channel retain ≈30% of the incident energy at $\theta_{inc}/\theta_{scat} = 25°$, which increases to ≈70% at $\theta_{inc}/\theta_{scat} = 65°$. By way of comparison, the IS energy retention fraction for CO_2 colliding with PFPE at $E_{inc} = 10.6$ kcal/mol is 49(4)% and 65(6)% for specular scattering at $\theta_{inc} = 30°$ and 60°, respectively. To first order, the CO_2 molecules and argon atoms retain approximately the *same* fraction of incident energy at a given incident angle when undergoing collisions through the IS pathway. In fact, based on the expected growth from our previous studies[17] in $\langle E_{scat}(IS) \rangle / E_{inc}$ with E_{inc}, the energy retention fraction for CO_2 is likely to increase, and may even exceed that of Ar, for studies at the *same* incident energy. Such a trend would suggest an

TABLE 4: Quantum Dopplerimetry Analysis of CO_2 Absorption Profiles

$\theta_{inc}-\theta_{scat}$							
0°−0°		30°−30°		45°−45°		60°−60°	
J	T_{trans} (K)	J	T_{trans} (K)	J	T_{trans} (K)	J	T_{trans} (K)
00^00 Translational Temperatures							
0	−[a]	0	370 (30)	0	390 (30)	0	480 (80)
2	−	2	380 (10)	2	400 (20)	2	470 (60)
4	−	4	360 (30)	4	400 (30)	4	480 (10)
6	−	6	360 (20)	6	440 (10)	6	450 (30)
8	−	8	370 (30)	8	410 (20)	8	440 (10)
10	−	10	360 (20)	10	420 (30)	10	440 (10)
12	−	12	370 (10)	12	450 (10)	12	470 (50)
14	350 (10)	14	380 (10)	14	440 (10)	14	490 (20)
16	370 (40)	16	360 (10)	16	460 (20)	16	500 (30)
18	400 (10)	18	410 (10)	18	470 (10)	18	550 (50)
20	430 (30)	20	400 (40)	20	480 (10)	20	550 (10)
22	460 (10)	22	420 (50)	22	480 (20)	22	540 (50)
24	460 (10)	24	420 (20)	24	540 (30)	24	610 (20)
26	500 (20)	26	450 (20)	26	570 (20)	26	620 (30)
28	490 (20)	28	490 (10)	28	580 (30)	28	700 (30)
30	520 (20)	30	490 (10)	30	610 (20)	30	720 (50)
34	570 (10)	34	530 (10)	34	720 (20)	34	710 (60)
36	570 (20)	36	570 (30)	36	710 (20)	36	770 (50)
38	600 (10)	38	610 (20)	38	770 (10)	38	840 (20)
40	620 (30)	40	640 (10)	40	770 (20)	40	840 (10)
42	640 (20)	42	670 (20)	42	840 (20)	42	940 (20)
44	630 (20)	44	680 (40)	44	850 (20)	44	940 (20)
46	680 (20)	46	650 (40)	46	890 (20)	46	990 (20)
50	700 (10)	50	760 (10)	50	920 (40)	50	1020 (10)
54	740 (40)	54	790 (40)	54	980 (60)	54	1030 (90)

[a] Absorption profiles for low J-states are not reported because of the contamination from the incident molecular beam.

initially counterintuitive result: energy transfer to the surface is less efficient for structured projectiles because of the propensity to convert collision energy into rotation of the CO_2.

One important dynamic difference is particularly worth noting. While the IS energy transfer efficiencies may be similar, CO_2 stores nearly one-third of its total recoil energy in rotation compared to Ar, where all energy is retained in translation. Thus, the internal degrees of freedom in CO_2 provide qualitatively new channels for redistribution of the incident translational energy, which would tend to increase $\langle E_{scat}(IS)\rangle/E_{inc}$. Physically, one can imagine a picture in which energy redistribution occurs through transient scattering into excited rotational states upon first collision at the gas−liquid interface, where the molecules then escape in an IS fashion via subsequent interaction(s) with the surface. On the other hand, such initial torque upon impact enhances the interaction time with the liquid, which quite likely enhances the efficiency of TD collisions that successfully dissipate their incident energy into the surface. Thus, for the same collision energy and incident angle, one might expect the trapping desorption fraction (α) to *increase* for structured (e.g., CO_2) versus unstructured (e.g., rare gas) projectiles, even though the fraction of molecules that do escape via the IS channel may carry away *more* energy per molecule. Clearly this is an area where molecular dynamics simulations are likely to be particularly useful in quantitatively interpreting these experimental observations.

A comparison to other state-resolved-scattering systems helps explore the role of translational-to-rotational energy transfer for CO_2. Several molecule−solid metal experiments provide a basis for comparison as well as contrast with the CO_2−liquid system. The progressions of rotational populations reveal "rotational rainbows" for a variety of metal scattering systems, which include N_2 from Ag(111),[41] HCl from Au(111),[46] and NO from Ag(111).[47−49] Although no such "rainbows" are observed for CO_2−liquid scattering, rotational excitation is a common path for energy transfer during the collision. For specular scattering at $\theta_{inc} = 45°$, the average CO_2 rotational energy increases from $\langle E_{rot}\rangle \approx 0.03$ kcal/mol in the supersonic molecular beam to $\langle E_{rot}\rangle \approx 1.3$ kcal/mol in the scattered flux. In a comparison to gas−metal systems, studies of HCl−Au(111) have revealed scattered species with $\langle E_{rot}\rangle \approx 1.3$ kcal/mol for a room-temperature surface at $E_{inc} = 17.9$ kcal/mol.[46] Despite differences in terms of rotational constants and incident collision energies, similar rotational excitation between these two systems illustrates a common motif of energy flow from translation into rotation of the scattered projectile during the gas−surface interaction.

While the magnitude of translational-to-rotational energy transfer may be comparable, the translational distributions of the scattered molecules do illustrate qualitative differences between the liquid and solid surfaces. Specifically, for each gas−solid metal system, molecules excited into *high* rotational states exhibit a *lower* translational kinetic energy. The strongly anticorrelated scattering behavior qualitatively contrasts with the results of CO_2 from PFPE, whereby *high* rotational states are also observed to be *highly* excited in translation as well. One must first consider whether such a trend in the present studies is complicated by mixed contributions from both TD and IS scattering. However, even after isolating the TD and IS fractions, this striking difference survives, as shown in Figure 6b where $T_{rot}(IS)$ essentially parallels $T_{trans}(IS)$ for all incident scattering angles. Such discrepancies between the gas−liquid and gas−solid scattering dynamics suggests different mechanisms for each type of interaction. Rigid-rotor hard-sphere and hard-cube models[55−60,71,72] have qualitatively reproduced the results for gas−solid metal-scattering systems, yet are unable to capture the trends in rotational populations observed in gas−liquid scattering.[17] The divergence of the two types of systems reflects many of the qualitative differences between the two surfaces, which includes how the local interaction environment changes a relatively smooth and hard solid to a much softer and potentially much rougher gas−liquid interface. Within this physical picture, we investigate alternative models that include

interactions beyond a single impulsive collision with a smooth surface site to uncover the mechanistic details associated with our two-temperature description of the scattering populations.

Characterization of the IS population with a temperature evokes a mechanism where single up to multiple gas−surface interactions play an important role in final scattering distributions of CO_2. While such a distribution of interactions is necessary to generate a temperature, it is worth noting that previous TOFMS studies have successfully modeled the IS channel as a *single* nonthermal interaction within a hard-sphere picture. For example, oxygen scattering from squalane displays broad final IS energy distributions that cannot be characterized by a Maxwell−Boltzmann function at any temperature.[13,14] Instead, a kinematic analysis of the average final O-atom velocities in a center-of-mass frame reveals that the oxygen ($E_{inc} = 11$ kcal/mol) collides inelastically with an effective surface mass (m_S) of 109 amu. When the model is corrected for internal excitation of the interacting surface fragment, hard-sphere collisions between oxygen and m_S quantitatively predict the fraction of energy transferred to the surface. These results indicate that the broad distributions observed reflect the large diversity in the local liquid surface environment. Similar distributions are ubiquitous throughout the majority of gas−liquid studies,[6,7] where the IS channel fails to emerge from the surface with any characteristic translational temperature.

While single interactions with highly corrugated surfaces may be responsible for the broad IS distributions typically measured in gas−liquid scattering, experiments by Flynn and Mullin have illustrated how single collisions produce both Boltzmann rotational and Maxwellian translational distributions for scattered CO_2 in the gas phase. When a room-temperature CO_2 interacts with vibrationally excited perfluorobenzene (C_6F_6),[73] the rotational state distributions of CO_2 (00^00) are Boltzmann and are well-characterized by a single rotational temperature of 795 K. As for translation, the absorption profiles are Gaussian with characteristic temperatures that range from 820 K for $J = 58$ to 1880 K for $J = 82$. While both degrees of freedom are characteristically Boltzmann-like, the highest *translational* temperatures reflect about twice the average energy stored in *rotation*. Note that this differs from the IS temperatures illustrated in Figure 6b, where T_{rot}(IS) is approximately *equal* to T_{trans}(IS) over the full range of incident angles. Further gas-phase studies of CO_2 with translationally hot H-atoms have illustrated that a single collision excites CO_2 (00^01) to a translational temperature of ≈1500 K, while only approximately three more gas kinetic collisions are able to relax CO_2 to a room-temperature distribution.[74] Though the above experiments probe purely gas-phase dynamics, the results provide additional support that CO_2 also scatters from the liquid after a small but finite number of interactions. Specifically, the experimental equivalence between T_{rot}(IS) and T_{trans}(IS) may signal a transient competition between collisional excitation and relaxation events, whose importance diminishes after approximately two to three collisions due to escape from the liquid surface.

By way of further validation, recent molecular dynamics simulations have compared CO_2 scattering from fluorinated self-assembled monolayers (F-SAMs)[39] with our experimental results for PFPE to gain insight into the fundamental physical interactions. In a direct comparison of rotational distributions, CO_2 scatters from F-SAMs with a characteristic temperature of T_{rot}(IS) = 765 K, which agrees remarkably well with our experimental value of 720(30) K. The molecular dynamics results show that CO_2 samples a wide range of interactions, from single "soft" collisions that yield thermally hot distributions,[32,39] to multiple collisions with a single surface site, as well as multiple collisions with different surface sites. Such a range of interactions likely contributes to a more microcanonical sampling of both rotational and translational degrees of freedom, which would begin to rationalize (i) a positive correlation between rotational/translational energy in the IS channel as well as (ii) a hyperthermal, but nevertheless more temperature-like, description of CO_2−PFPE scattering distributions.

V. Conclusion and Summary

Quantum-state-resolved dynamics of carbon dioxide and perfluorinated liquids continue to uncover physical insights into the fundamental interactions between a gas and liquid surface. The laser-based detection scheme complements the enormous efforts of TOFMS experiments and high-level theoretical simulations. The central themes discovered in previous studies continue to be reinforced at the quantum state level. Specifically, the incident angle of the projectile determines the probability (α) of trapping through energy deposition into the surface. As θ_{inc} increases, the observed trends include a decrease in the TD population, increased excitation in both rotation and translation, and yet no change in the magnitude of the vibrational excitation. These trends are consistent with finite interaction times for molecules in the IS channel, where facile translational-to-rotational excitation is achieved, yet with insufficient temporal duration to facilitate the translational-to-vibrational transfer of even relatively low-frequency CO_2 bending vibrational quanta. Further insight into this time scale is provided by the hyperthermal Boltzmann-like description of populations that have been isolated in the nominally impulsive IS channel. The isolated IS temperatures most likely reflect the effect of multiple "soft" single collisional interactions in the scattering event, which provides a sufficiently microcanonical sampling of rotational/translational energies in the scattered CO_2 to achieve distributions well characterized by a common, albeit hyperthermal, temperature.

Acknowledgment. Support for this work is provided by the Air Force Office of Scientific Research. Additional funds from the National Science Foundation are also gratefully acknowledged. We would like also to acknowledge the stimulation and many valuable scientific discussions that the Miller and Nesbitt groups have enjoyed over the years, as well as our deep sadness that we have all lost such an experimental prince of the scientific community.

References and Notes

(1) Saecker, M. E.; Govoni, S. T.; Kowalski, D. V.; King, M. E.; Nathanson, G. M. *Science* **1991**, *252*, 1421.
(2) Saecker, M. E.; Nathanson, G. M. *J. Chem. Phys.* **1993**, *99*, 7056.
(3) Saecker, M. E.; Nathanson, G. M. *J. Chem. Phys.* **1994**, *100*, 3999.
(4) King, M. E.; Saecker, M. E.; Nathanson, G. M. *J. Chem. Phys.* **1994**, *101*, 2539.
(5) King, M. E.; Nathanson, G. M.; Hanninglee, M. A.; Minton, T. K. *Phys. Rev. Lett.* **1993**, *70*, 1026.
(6) Nathanson, G. M.; Davidovits, P.; Worsnop, D. R.; Kolb, C. E. *J. Phys. Chem.* **1996**, *100*, 13007.
(7) Nathanson, G. M. *Annu. Rev. Phys. Chem.* **2004**, *55*, 231.
(8) Manning, M.; Morgan, J. A.; Castro, D. J.; Nathanson, G. M. *J. Chem. Phys.* **2003**, *119*, 12593.
(9) Ringeisen, B. R.; Muenter, A. H.; Nathanson, G. M. *J. Phys. Chem. B* **2002**, *106*, 4999.
(10) Ringeisen, B. R.; Muenter, A. H.; Nathanson, G. M. *J. Phys. Chem. B* **2002**, *106*, 4988.
(11) King, M. E.; Fiehrer, K. M.; Nathanson, G. M.; Minton, T. K. *J. Phys. Chem. A* **1997**, *101*, 6556.
(12) Minton, T. K.; Tagawa, M.; Nathanson, G. M. *J. Spacecr. Rockets* **2004**, *41*, 389.

(13) Zhang, J.; Garton, D. J.; Minton, T. K. *J. Chem. Phys.* **2002**, *117*, 6239.
(14) Minton, T. K.; Garton, D. J. Dynamics of Atomic-Oxygen-Induced Polymer Degradation in Low Earth Orbit. In *Chemical Dynamics in Extreme Environments*; Dressler, R. A., Ed.; World Scientific Publishing Co.: Singapore, 2001; p 420.
(15) Kelso, H.; Kohler, S. P. K.; Henderson, D. A.; McKendrick, K. G. *J. Chem. Phys.* **2003**, *119*, 9985.
(16) Kenyon, A. J.; McCaffery, A. J.; Quintella, C. M.; Zidan, M. D. *Chem. Phys. Lett.* **1992**, *190*, 55.
(17) Perkins, B. G.; Nesbitt, D. J. *J. Phys. Chem. B* **2006**, *110*, 17126.
(18) Zolot, A. M.; Harper, W. W.; Perkins, B. G.; Dagdigian, P. J.; Nesbitt, D. J. *J. Chem. Phys.* **2006**, *125*, 021101.
(19) Perkins, B. G.; Haber, T.; Nesbitt, D. J. *J. Phys. Chem. B* **2005**, *109*, 16396.
(20) DuPont "Krytox Fluid Performance Sheets," 2003.
(21) Sinha, M.; Fenn, J. *Proceedings of the 5th International Symposium on Molecular Beams*, 1975, Nice, France.
(22) Morris, J. R.; Behr, P.; Antman, M. D.; Ringeisen, B. R.; Splan, J.; Nathanson, G. M. *J. Phys. Chem. A* **2000**, *104*, 6738.
(23) Castro, D. J.; Dragulin, S. M.; Manning, M.; Nathanson, G. M. *J. Chem. Phys.* **2006**, *125*, 144715.
(24) Muenter, A. H.; DeZwaan, J. L.; Nathanson, G. M. *J. Phys. Chem. B* **2006**, *110*, 4881.
(25) Morgan, J. A.; Nathanson, G. M. *J. Chem. Phys.* **2001**, *114*, 1958.
(26) Day, B. S.; Shuler, S. F.; Ducre, A.; Morris, J. R. *J. Chem. Phys.* **2003**, *119*, 8084.
(27) Day, B. S.; Morris, J. R. *J. Phys. Chem. B* **2003**, *107*, 7120.
(28) Scott Day, B.; Morris, J. R.; Troya, D. *J. Chem. Phys.* **2005**, *122*, 214712.
(29) Ferguson, M. K.; Lohr, J. R.; Day, B. S.; Morris, J. R. *Phys. Rev. Lett.* **2004**, *92*, 073201.
(30) Gibson, K. D.; Isa, N.; Sibener, S. J. *J. Chem. Phys.* **2003**, *119*, 13083.
(31) Yan, T. Y.; Isa, N.; Gibson, K. D.; Sibener, S. J.; Hase, W. L. *J. Phys. Chem. A* **2003**, *107*, 10600.
(32) Isa, N.; Gibson, K. D.; Yan, T.; Hase, W.; Sibener, S. J. *J. Chem. Phys.* **2004**, *120*, 2417.
(33) Rosenbaum, A. W.; Freedman, M. A.; Darling, S. B.; Popova, I.; Sibener, S. J. *J. Chem. Phys.* **2004**, *120*, 3880.
(34) Bosio, S. B. M.; Hase, W. L. *J. Chem. Phys.* **1997**, *107*, 9677.
(35) Yan, T. Y.; Hase, W. L. *J. Phys. Chem. B* **2002**, *106*, 8029.
(36) Yan, T. Y.; Hase, W. L.; Barker, J. R. *Chem. Phys. Lett.* **2000**, *329*, 84.
(37) Yan, T. Y.; Hase, W. L. *Phys. Chem. Chem. Phys.* **2000**, *2*, 901.
(38) Troya, D.; Schatz, G. C. *J. Chem. Phys.* **2004**, *120*, 7696.
(39) Martinez-Nunez, E.; Rahaman, A.; Hase, W. L. *J. Phys. Chem. C* **2007**, *111*, 354.
(40) Lipken, N.; Gerber, R. B.; Moiseyev, N.; Nathanson, G. M. *J. Chem. Phys.* **1994**, *100*, 8408.
(41) Sitz, G. O.; Kummel, A. C.; Zare, R. N. *J. Chem. Phys.* **1988**, *89*, 2558.
(42) Sitz, G. O.; Kummel, A. C.; Zare, R. N.; Tully, J. C. *J. Chem. Phys.* **1988**, *89*, 2572.
(43) Kummel, A. C.; Sitz, G. O.; Zare, R. N.; Tully, J. C. *J. Chem. Phys.* **1988**, *89*, 6947.
(44) Kummel, A. C.; Sitz, G. O.; Zare, R. N.; Tully, J. C. *J. Chem. Phys.* **1989**, *91*, 5793.
(45) Lykke, K. R.; Kay, B. D. *J. Phys.: Condens. Matter* **1991**, *3*, S65.
(46) Lykke, K. R.; Kay, B. D. *J. Chem. Phys.* **1990**, *92*, 2614.
(47) Rettner, C. T.; Kimman, J.; Fabre, F.; Auerbach, D. J.; Barker, J. A.; Tully, J. C. *J. Vac. Sci. Technol., A* **1987**, *5*, 508.
(48) Rettner, C. T.; Kimman, J.; Auerbach, D. J. *J. Chem. Phys.* **1991**, *94*, 734.
(49) Kubiak, G. D.; Hurst, J. E.; Rennagel, H. G.; McClelland, G. M.; Zare, R. N. *J. Chem. Phys.* **1983**, *79*, 5163.
(50) Asada, H. *Jpn. J. Appl. Phys.* **1981**, *20*, 527.
(51) Wight, A. C.; Penno, M.; Miller, R. E. *J. Chem. Phys.* **1999**, *111*, 8622.
(52) Wight, A. C.; Miller, R. E. *J. Chem. Phys.* **1998**, *109*, 8626.
(53) Wight, A. C.; Miller, R. E. *J. Chem. Phys.* **1998**, *109*, 1976.
(54) Francisco, T. W.; Camillone, N.; Miller, R. E. *Phys. Rev. Lett.* **1996**, *77*, 1402.
(55) Doll, J. D. *J. Chem. Phys.* **1973**, *59*, 1038.
(56) Logan, R. M.; Stickney, R. E. *J. Chem. Phys.* **1965**, *44*, 195.
(57) Nichols, W. L.; Weare, J. H. *J. Chem. Phys.* **1977**, *66*, 1075.
(58) Nichols, W. L.; Weare, J. H. *J. Chem. Phys.* **1975**, *62*, 3754.
(59) Nichols, W. L.; Weare, J. H. *J. Chem. Phys.* **1975**, *63*, 379.
(60) Park, S. C.; Bowman, J. M. *J. Chem. Phys.* **1984**, *80*, 2183.
(61) Bowman, J. M.; Park, S. C. *J. Chem. Phys.* **1982**, *77*, 5441.
(62) Proch, D.; Trickl, T. *Rev. Sci. Instrum.* **1989**, *60*, 713.
(63) Lednovich, S. L.; Fenn, J. B. *AIChE J.* **1977**, *23*, 454.
(64) Kaur, D.; Desouza, A. M.; Wanna, J.; Hammad, S. A.; Mercorelli, L.; Perry, D. S. *Appl. Opt.* **1990**, *29*, 119.
(65) The notation ($\nu_1\nu_2^l\nu_3$) characterizes the vibrational state of CO_2; the quantum numbers ν_1, ν_2, and ν_3 describe the symmetric stretch, bend, and antisymmetric stretch, and l is the vibrational angular momentum quantum number.
(66) Miller, D. R. Free Jet Sources. In *Atomic and Molecular Beam Methods*; Scoles, G., Ed.; Oxford University Press: New York, 1988; Vol. 1, p 14.
(67) Zacharias, H.; Loy, M. M. T.; Roland, P. A.; Sudbo, A. S. *J. Chem. Phys.* **1984**, *81*, 3148.
(68) Nizkorodov, S. A.; Harper, W. W.; Chapman, W. B.; Blackmon, B. W.; Nesbitt, D. J. *J. Chem. Phys.* **1999**, *111*, 8404.
(69) Headgordon, M.; Tully, J. C.; Rettner, C. T.; Mullins, C. B.; Auerbach, D. J. *J. Chem. Phys.* **1991**, *94*, 1516.
(70) Goodman, F. O.; Wachman, H. Y. *Dynamics of Gas-Surface Scattering*; Academic Press: New York, 1976.
(71) Bowman, J. M.; Park, S. C. *J. Chem. Phys.* **1982**, *77*, 5441.
(72) Tully, J. C. *J. Chem. Phys.* **1990**, *92*, 680.
(73) Michaels, C. A.; Lin, Z.; Mullin, A. S.; Tapalian, H. C.; Flynn, G. W. *J. Chem. Phys.* **1997**, *106*, 7055.
(74) Hershberger, J. F.; Chou, J. Z.; Flynn, G. W.; Weston, R. E. *Chem. Phys. Lett.* **1988**, *149*, 51.
(75) Cohen, S. R.; Naaman, R.; Sagiv, J. *J. Chem. Phys.* **1988**, *88*, 2757.